Chemical Science

ROYAL SOCIETY OF CHEMISTRY

EDGE ARTICLE

View Article Online
View Journal | View Issue

Cite this: *Chem. Sci.*, 2023, **14**, 6654

All publication charges for this article have been paid for by the Royal Society of Chemistry

Received 15th April 2023
Accepted 24th May 2023

DOI: 10.1039/d3sc01960h

rsc.li/chemical-science

Isotope-encoded tetrahedral DNA for multiple SARS-CoV-2 variant diagnosis†

Ziyan Li,[a] Jing Zhou,[a] Chaoqun Wang,[a] Rui Liu,*[b] Jianyu Hu[c] and Yi Lv*[ab]

The evolution of severe acute respiratory syndrome coronavirus 2 (SARS-CoV-2) has posed an unprecedented demand for accurate and cost-effective diagnostic assays to discriminate between different variants. Whilst many bioassays have been successfully demonstrated for SARS-CoV-2 detection, diagnosis of its variants remains challenging and mainly relies on time-consuming and costly sequencing techniques. Herein, we proposed a triplevalent tetrahedral DNA nanostructure (tTDN) with three overhang isotope probes capable of multiplex simultaneous analysis. HV69/70 del (alpha-specific), K417N (beta-specific) and T478K (delta-specific) and omicron with common mutations above of the SARS-CoV-2 S gene were detected selectively with the aid of the TDN scaffold and MNAzyme system, and a sensitive strategy enabling the screening of four kinds of variants of concern (VOC) was achieved.

Introduction

Multiple variants of SARS-CoV-2 (ref. [1]) have shown increased transmissibility and pathogenicity.[2] The Centers for Disease Control and Prevention (CDC) has now defined five strains of SARS-CoV-2 alpha/beta/gamma/delta/omicron as VOC,[3] with the necessity for strict monitoring. These remarkable mutations, including HV69-70del, K417N, and T478K, all occur in the major transmembrane spike (S) glycoprotein,[4–6] enhancing the ability of the virus to invade cells or contribute to the immune escape of the virus.[7] Population scale sweeps of multiple SARS-CoV-2 variants brought new challenges for molecular diagnostics and widespread availability of multiplexed, scalable diagnostic screening for the SARS-CoV-2 variant is required to enable active surveillance and focused patient care.[8]

The mainstream for pathogen genomic surveillance is whole genomic sequencing (WGS),[9] while it calls for long turnaround times, especially in the screening of multiple variants.[10] The quantitative reverse-transcription polymerase chain reaction (qRT-PCR) assays provide the greatest sensitivity and specificity to implement,[11] but still shortages of supplies and laboratory personnel exist, and most of these assays either target a single mutation per response or lack sufficient targets for thoroughly characterizing SARS-CoV-2.[12] Crucially, tied up by the spectral overlap of fluorescent tags,[13] implementations of existing multiplex sequencing[14] and PCR[15] strategies for SARS-CoV-2 variant diagnosis rely on microarrays[14,16] or pre-separations[12,17] that are essentially a sum of multiple assays after aliquoting each sample. For key mutations in the virus, a new genotyping method needs to be developed that is more efficient and multiplexable than WGS. Scalable diagnostic tools to efficiently detect multiple variants of SARS-CoV-2 in a single tube are still lacking.

Intriguingly, molecular interpretations encoded by multiple isotopes exhibit high sensitivity, wide dynamic range,[18] and, most importantly, no signal overlap compared to most used fluorophore tags.[19,20] Efforts have been made in multiplexed assays with respect to nucleic acid[21,22] and protein[23,24] markers for molecular diagnostics, and mass cytometry (CyTOF),[25] spatial single nuclear metabolomics (SEAM)[26] have showcasted superior high-dimensional barcoding ability. Overall, isotope-encoding mass spectrometry is ideally suited for multicomponent assays.

To address the need for affordable and accessible multiplexity, a tTDN-magnetic bead (MB) satellite with lanthanide isotope tags at the vertices was constructed for the detection of multi-component character mutations. The TDN provides an oriented scaffold[27–31] for subsequent reaction design, which is a ubiquitous method for tracing biological analytes owing to its relatively high sensitivity[32,33] and easily fabricated features.[34–36] Furthermore, its distinctive multi-vertex structure[37–40] makes it an ideal platform for multi-component bioanalysis.[40–42] Combining the advantages of TDN and mass spectrometry, a multi-tentacle tTDN with overhang lanthanide isotope probes as MNAzyme substrates for multiplex analysis of HV69/70 del (alpha-specific), K417N (beta-specific) and T478K (delta-specific)[3] was established. The tTDN on MBs provides well-

[a]*Analytical & Testing Center, Sichuan University, Chengdu 610064, China. E-mail: lvy@scu.edu.cn*

[b]*Key Laboratory of Green Chemistry & Technology, Ministry of Education, College of Chemistry, Sichuan University, Chengdu 610064, Sichuan, China. E-mail: liur@scu.edu.cn*

[c]*Division of Analytical and Environmental Toxicology, Faculty of Medicine & Dentistry, University of Alberta, Edmonton T6G 2G3, Alberta, Canada*

† Electronic supplementary information (ESI) available. See DOI: https://doi.org/10.1039/d3sc01960h

controlled nanoscale distance,[43] efficiently reducing the non-specific adsorption of the overhang probe DNA. The splicing of the overhang probe by MNAzyme[44] could fulfil the re-release of RNA together with isotope tags which are continuously peeled off like satellites in orbit, achieving signal amplification.

The tTDN accelerates the MNAzyme reaction kinetics[45] compared to ssDNA probes due to the synergistic contributions of stereo distance and specific reaction orientations, moreover, exhibiting biostability and multiplicity.[38] As a proof-of-concept, it is a promising candidate for screening of SARS-CoCV-2 VOC variants.

Experimental

Materials and apparatus

A PerkinElmer NexION 350 inductively coupled plasma mass spectrometer was used throughout the experiments. The ESI† contains a comprehensive list of the parameters of ICPMS (Table S1†), nucleotide sequences (Table S2†), chemicals, reagents, and some of the operational procedures and characterizations studies.

Labeling of HV69/70 del, K417N, and T478K-substrates with Tb, Ho and Tm

The labeling process was first conducted with protocols adopted from the previous work of Wang's group.[46] Fig. 1a depicts a diagrammatic sketch of the technique, with individual operations provided in the ESI.† In accordance with that, 1,4,7,10-tetraazacyclodo-decane-1,4,7-tris-acetic acid-10-maleimidoethylacetamide (MMA-DOTA) forms a chelate complex with a lanthanide(III) ion Tb^{3+}/Ho^{3+}/Tm^{3+} and finally we got the DNA-MMA-DOTA-Tb^{3+}/Ho^{3+}/Tm^{3+} conformations.

Preparation of the tTDN using the thermal annealing protocol

Each of the three isotope-labeled DNA tracks, as well as a biotin-labeled DNA (t-T) as the fourth backbone of the tTDN structure, was diluted to 8 μM. At a final concentration of 2 μM, equal molar quantities of the composition DNA strands were mixed in TM buffer. The mixed strands were heated to 90 °C for 5 minutes before being cooled gradually to 4 °C, remaining for at least 15 min on a K960 Thermal Cycler (Heal Force Inc., China).

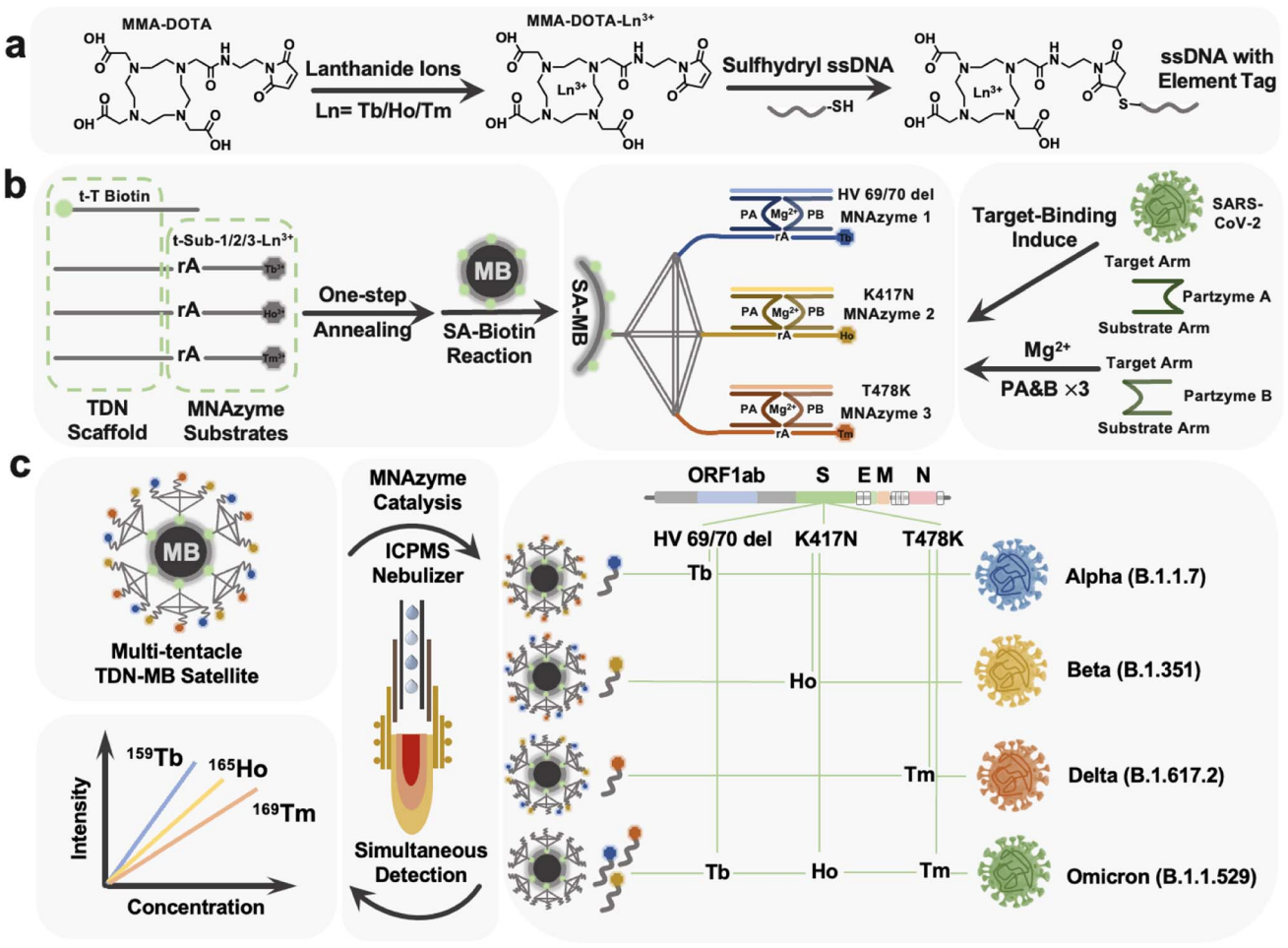

Fig. 1 tTDN–MNAzyme sensor for SARS-CoV-2 RNA mutation detection. (a) The procedure for labeling track strands with lanthanide tags. (b) Schematic illustration of the assembly of the MBs–Tb–Ho–Tm tTDN–MNAzyme satellite and the mechanism for MNAzyme catalysis. (c) Viral genome map, and targeted regions of the three isotope probes. Workflow of multiple mutated RNA fragment detection of HV69/70 del, K417N and T478K with regard to variants alpha, beta, delta, and omicron with ICPMS.

Preparation of triple probe tTDN–MB satellites

The reactant material employed was a type of commercially available, 1 mm diameter magnetic bead that had the surface of the bead modified with SA (Fig. S5†). 100 μL of SA–MBs were pre-washed with TM buffer before usage and then mixed with 500 μL of prepared 2 M tTDN. The triple probe tTDN–MB satellites were produced when the mixture was incubated for one hour at room temperature with gentle shaking to immobilize DNA on the surface through a particular binding between SA and biotin on tTDN. The tTDN–MB satellites were then washed three more times with TMR buffer for later use after being rinsed with TM buffer to remove extra unreacted DNA. These tTDN–MB satellites in TMR were made up to a final volume of 1 mL in case of usage.

Multiplex assay procedure of HV69/70 del, K417N, and T478K based on the tTDN–MNAzyme nanosystem

The multiplex assay procedure of HV69/70 del, K417N, and T478K through tTDN–MB satellites based on the tTDN–MNAzyme nanosystem was made up of several components. Partzyme A and partzyme B for every MNAzyme were previously dissolved in TMR buffer to 1 μM and 5 μL of each was taken; 10 μL of the prepared tTDN–MB satellites was adapted. The addition amount of the analyte samples with different concentrations is unified to 10 μL; finally the volume of the whole tTDN–MNAzyme nanosystem was replenished with TMR to 100 μL. At a temperature of 37 °C, the nanosystem was gently shaken for 3 h to fully react and make the isotope probe entirely sheared.

Viral RNA extraction for the standard recovery experiment

Throat swab samples were used to create the real sample matrix for the recovery experiment, which was then purified using the EZ-10 spin column viral total RNA extraction kit. In the ESI,† specific experimental procedures are described.

ICPMS measurements

After magnetic separation, the total volume of reactants and products in the supernatant was 100 μL per tube. It was then diluted with 1% HNO_3 to a final volume of 1 mL and measured by ICPMS with Tb, Ho, and Tm isotopes in simultaneous detection mode.

Results and discussion

Assay overview

Based on the constructed MNAzyme mediated tTDN–MB satellite model, we have created a multiplex detection approach for SARS-CoV-2 variant-related RNA fragments that transforms an RNA molecule into numbers of free lanthanides. The nanosatellite model consists of the MB core and tTDN scaffold with three MNAzyme modules (Fig. 1b). (1) MBs: they offer a platform for and a means of separating heterogeneous biological reactions, as well as a sizable specific surface area to facilitate maximal arrangement of tTDN structures. (2) tTDN: tTDN consists of four chains. One was designed with biotin modification at the 5′ end for connecting to SA–MBs (t-toehold), and at the same time, the toe chain was lengthened with 5 T bases, partially preventing SA–biotin binding from tTDN's steric hindrance. A branched tTDN (Fig. 1b), which exhibits a satellite-like structure on the surface of the MBs and acts as a stiff scaffold for functionalized branch chains to sprout, is made up of both the T-toehold and three other longer chains, t-substrate. Three t-substrates with middle-cleavage site modifications (rA) and 3′ ends modified with various lanthanides to produce appropriate ICPMS signals are present on each branching strand. (3) MNAzyme system: each MNAzyme system is made up of three parts: a pair of partzymes A & B, a substrate from the tTDN branch, and a target for initiating the assembly of the MNAzyme structure. When the analyte is present, the free partzymes A & B are drawn closer by the complementary pairing rule and further allow the other part of partzymes A & B to bind to the substrate.

Under the synergistic influence of the Mg^{2+}, the active center can cleave the tTDN branched substrate chain at the rA site. The MNAzyme structure is less sterically hindered by the tTDN structure and more likely to collide with the three t-substrates since there is a gap of 5 T bases between the sequences that participate in the structure and the sequences acting as substrates. Due to thermal instability, the sheared lanthanide-labelled DNA fragments are released into the solution, and the entire MNAzyme system can then be released once more, liberated, and located for the subsequent t-substrate for cleaving to provide isotope signals. As a result, three t-substrates serve as sites for the labelling of lanthanide tags, substrates for MNAzymes, and parts of the tTDN structure.

As triggers for the tTDN–MNAzyme nanosystem, we investigated three characteristic RNA sequences (HV69/70 del, K417N, and T478K) associated with four VOC SARS-CoV-2 variants. Three RNAs were concurrently added to the nanosystem containing tTDN, as seen in Fig. 1c, and this initiated the reaction, releasing significant amounts of the three lanthanides into the supernatant. ICPMS was used to identify the three lanthanide signals. For the purpose of identifying and determining SARS-CoV-2 variations, HV69/70 del is the indicative gene of the alpha variant, K417N is descriptive of the beta variant, and T478K is symptomatic for the gamma variant. It is noteworthy that all the aforementioned mutation sites are present in the recently discovered omicron variants. As a result, we can quantify the characteristic sequence of the variation and identify the relevant SARS-CoV-2 variants based on the combination and intensity of the isotope signals in ICPMS.

Characterization of the tTDN–MB satellites

To verify the successful formation of tTDN, we characterized by atomic force microscopy (AFM) (Fig. 2a), PAGE, and dynamic light scattering (DLS) (Fig. 2d and S4†). In PAGE, a single strand of tTDN building blocks, a dimer and a trimer were adapted with the same annealing procedure as tTDN formation. The gradual increase in molecular weight demonstrated the binding of several strands (Fig. 2c). Furthermore, in the AFM image, ssDNA is dispersed and soft, while tTDN has a certain rigidity

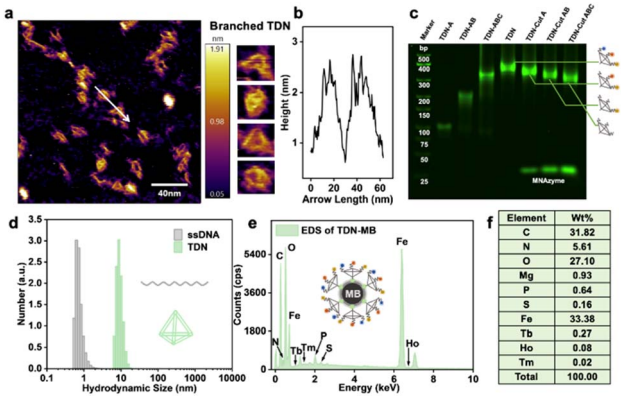

Element	Wt%
C	31.82
N	5.61
O	27.10
Mg	0.93
P	0.64
S	0.16
Fe	33.38
Tb	0.27
Ho	0.08
Tm	0.02
Total	100.00

Fig. 2 (a) Atomic force microscope (AFM) image of the tTDN accompanied by the enlarged images. (b) The cross-sectional profile of the tTDN, which was taken along the white line in (a). (c) Characterization of the formation of tTDN by PAGE. From lanes left to right: marker, single strand, dimer, trimer, complete tTDN, single/double/triple components product tTDN after the MNAzyme reaction. (d) DLS analysis of ssDNA and tTDN prepared using 500 nM compositional strands. (e) EDS spectrum of the as-synthesized isotope tTDN attached on MBs. (f) Weight content distribution of elements in EDS.

and maintains a three-dimensional structure (Fig. S3†). In a finer view, the tetrahedral structure can be clearly observed (Fig. 2a). The cross-sectional profile of the tTDN, which was taken along the white line, shows a clear height variation at the location of the tTDN (Fig. 2b). The aqueous ssDNA solution's hydrated particle size is approximately 1 nm, but after combining with tTDN, the hydrated particle size increases to 10 nm. In Fig. 2d and S4,† the particle size distribution indicates that the synthesized tTDN is comparatively pure and homogeneous. Evidence demonstrates the formation of tTDN from a more intuitive perspective.

The MB ingredients are Fe_3O_4 with SA on the surface; tTDNs are immobilized onto the MBs through the SA–biotin linkage. The sphere becomes positively charged overall thanks to SA, and after tTDN was attached, its negative charge (essentially as DNA) replaces the positive charge on the particle surface (Fig. S6†). In isotope analysis by energy dispersive spectroscopy (EDS) (Fig. 2e, f and S7†), MBs contain a large amount of C, N, O, P, S and Fe elements. When the isotope-labeled tTDN was coupled to the MBs, we discovered newly emerged elements: Mg, Tb, Ho and Tm. This not only demonstrates the labeling of the single strand by the lanthanide isotope but also the successful assembly of the four single strands into tTDN and their further immobilization.

Feasibility of the tTDN–MNAzyme nanosystem. The three lanthanide metal nitrate standards that were employed as isotope labels were first subjected to a series of gradient dilutions in order to produce standard curves for the simultaneous measurement of the three isotopes in ICPMS (Fig. S8†). The findings demonstrate that the ICPMS response to Tb, Ho, and Tm exhibits strong linearity, which is necessary for our devised approach to be able to quantify multiple SARS-CoV-2 variants' RNA fragments.

To test the feasibility of the developed tTDN–MNAzyme nanosystem, ICPMS detection under different conditions was done (Fig. S14†). In the absence of ingredients, no reaction and release of isotope tags will occur. Only when partzymes A & B exist and accompanied by Mg^{2+} ions, the tTDN–MB satellite will release the isotope tag under the initiation of the target. And the occurrence of the reaction depends on the type and quantity of the target. In Fig. 2c, the branching t-substrate chains of TDNs were spliced by 1–3 sites when we introduced the same amount of 1–3 kinds of variant RNAs, and the molecular weight of tTDN dropped with the number of splices. This demonstrates the feasibility of the tTDN–MNAzyme nanosystem to operate from single to multiple components.

Optimization of experimental conditions

In theory, each type of capture DNA strand accounted for one-third of the total attached capture DNA. Therefore, we took one component as an indicator, optimized the relevant experimental conditions, and extended the results to the three-component analysis. The main contents include the assembly process of tTDN and MBs and the reaction conditions of MNAzyme.

Preparation process of the tTDN. Both the thermal annealing protocol[47] and snap cooling protocol[48] are widely used for preparing the tTDN, and before establishing an analytical nanosystem, we previously made an inquiry of the stability of tTDN through these two ways. Upon treatment without/with a certain amount of DNase I and subsequently a PAGE experiment, we found that tTDN prepared using the thermal annealing protocol exhibits better stability (Fig. S9†). Therefore, we adopted this synthesis method in subsequent experiments.

Reaction platform. Before starting the experiment, we first carried out the selection of the reaction platform and the loading of tTDN on the platform. Commonly used heterogeneous biological reaction substrates include MBs and microplates. Taking the total binding amount of isotope-tagged tTDN as a criterion, both SA–MBs and SA-96 well microplates were compared. The results are shown in Fig. S10.† Under the same conditions, the magnetic beads have a larger specific surface area, which is more conducive to the spatial dispersion of tTDN with a rigid structure and more binding.

tTDN–MB incubation buffer. Furthermore, we optimized the buffer for tTDN magnetic beads. In previous protocols, high-salt buffers were often adopted, because the environment of high ionic strength can make biotinylated nucleic acid molecules more rigid and can "stand" on the surface of magnetic beads for more efficient binding. However, the frame structure of the tTDN molecule used in our scheme already has a certain rigidity, and the sudden change of ionic strength may instead destroy its original structure. From the results in Fig. S11,† we finally chose the original TM buffer for tTDN formation.

tTDN–MB ratio. According to the instructions, 5000 pmol of ssDNA can be loaded on 1 mL SA–MBs. To achieve a better analytical performance and make the MBs saturated and feasible for tTDN binding with minimal waste, we altered the addition amount. Therefore, we tried loading SA–MBs 2.5, 5, 7.5, 10, and 12.5 times and found that 5 times is sufficient.

Amount of tTDN–MBs. After preparing MBs fully coated with tTDN, we tried to explore the amount of tTDN–MBs in each

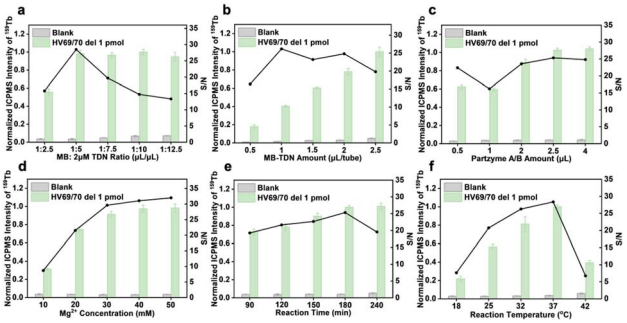

Fig. 3 Optimization of experimental conditions. (a) tTDN–MB ratio. (b) Amount of tTDN–MBs. (c) Amount of partzymes A/B for the formation of MNAzymes. (d) Amount of Mg^{2+} for the cleavage of substrates. (e) Reaction time and (f) temperature for the multiplex assay using the tTDN–MNAzyme nanosystem.

sample. The results showed that tTDN–MBs of 0.5–2.5 all exhibited similar signal-to-noise ratios in the analysis process, and the signal increased exponentially with the dosage. However, less dosage might cause it difficult to observe the collection and dispersion of the MBs when washing and removing the supernatant, which is easy to cause loss of MBs. Additionally, we talked about the tTDN–MBs' incubation period in detail, as illustrated in Fig. S12.†

Amount of partzyme A/B for the formation of MNAzymes. The primary MNAzyme components, partzyme A and partzyme B, largely provided two partial catalytic core parts to form a complete catalytic core and endowed the assembled MNAzymes with cleavage activity. In order to achieve the best results, the amount of the partzymes A & B was varied between 0.5 and 4 μL, 1 μM. Fig. 3c shows that the signals grew quickly as partzyme A/B concentration increased from 0.5 to 2 μL and stayed nearly constant and gained the best S/N ratio as partzyme A/B climbed to 2.5 μL, 1 μM.

Amount of Mg^{2+} for the cleavage of substrates. Mg^{2+} plays a crucial function in aiding MNAzymes, as seen in Fig. 1b, making it a necessary component of tTDN–MB satellites. Investigated were the effects of Mg^{2+} concentrations ranging from 10 to 50 mM (Fig. 3d) and 30 to 70 mM (Fig. S13†). The detection signal rose dramatically from 10 to 40 mM Mg^{2+} concentrations but did not differ significantly between 50 and 70 mM (Fig. S13†), showing that 50 mM was adequate to support the MNAzyme. The Mg^{2+} concentration utilized in subsequent trials was 50 mM.

Reaction time for the multiplex assay using the tTDN–MNAzyme nanosystem. A frequent circumstance that significantly affects the effectiveness of reactions is the hybridization time. As shown in Fig. 4e, we investigated the reaction efficiency in the time range of 90–240 min in order to ensure sufficient time and control nonspecific adsorption. When both signal growth and blank control are taken into account, the signal value initially exhibits an upward trend and then gradually stabilizes, but the blank value initially declines due to the target molecule's competition and then increases over time. We determine that 180 minutes is the optimal hybridization time.

Reaction temperature for the multiplex assay using the tTDN–MNAzyme nanosystem. We studied the appropriate temperature for the interaction. When the chosen reaction temperature is below the target sequence's melting temperature (T_m, ~50 °C), which ranges from 15 to 20 °C, the reaction will be more effective for the same reaction time; the lower the temperature, the more stable the double-stranded binding DNA will be. As seen in Fig. 4f, we have created a number of hybridization temperatures to investigate the interplay between these two parameters. The best signal-to-noise ratio can be

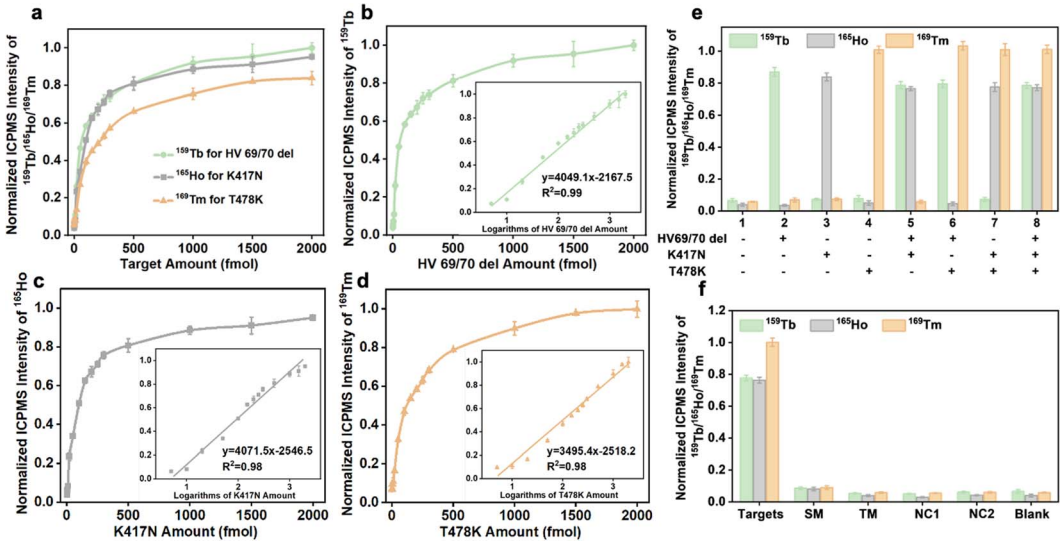

Fig. 4 (a) Signal response for different concentrations of targets (b) HV 69/70 del, (c) K417N, and (d) T478K. Inset graphs show the calibration plots of the ICPMS signal intensity *versus* the logarithmic RNA concentration. Error bars represent the standard deviations of three independent measurements. (e) Cross-reactivity, and (f) selectivity in the cases of 1 pmol target and single-base mismatch RNAs, triple-base mismatch RNAs, and non-complementary miRNAs with the concentration of 10 pmol.

attained when the temperature is 37 °C. Finally, it was determined that 37 °C was the ideal reaction temperature.

Analytical performance

The analytical performance of the established analytical method after optimizing a number of reaction conditions was studied. In the simultaneous detection strategy, the calibration curves were constructed utilizing varying amounts of RNA fragments (HV69/70 del, K417N, and T478K) and ICPMS signal intensities of lanthanide isotopes (^{159}Tb/^{165}Ho/^{169}Tm). Three different target types can be combined and quantified, as seen in Fig. 4a, indicating similar tendencies and performance. After executing logarithmic processing and linear fitting of the data, a good linear relationship for HV69/70 del, K417N, and T478K was found at 5–2000 fmol in the inset figures of Fig. 4b–d, and the correlation equations are shown in Table 1. The limits of detection calculated from $3\sigma/k$ ($n = 10$) for HV69/70 del, K417N, and T478K were 1.2, 1.5, and 1.1 fmol, respectively.

The branched tTDN not only participates in the multi-component reaction but also acts as a rigid molecular scaffold, making the overhang probe more oriented. This is because it spatially keeps the probe away from the MB surface, avoiding the electrostatic adsorption of long ssDNA on the MB surface to a certain extent (Fig. 5a). Obviously, the tTDN-based MNAzyme multiplex strategy possesses better analytical performance than the ssDNA probe. Fig. 5b displays how they performed in the wide range of multi-component detection. We discovered that the isotope signal growth rates of the two are comparable at low analyte concentrations. This is due to their adequate quantity, which facilitates a positive shift in the reaction equilibrium, which is significantly more than the analyte. Above 250 fmol of targets, the ssDNA probes were plainly not enough to handle more targets, and the reaction quickly reached a plateau since it was unable to carry out biological duties as a result of adsorption and entanglement. tTDN's triple probe overhang, however, is supported by a rigid scaffold that is less constrained than ssDNA, allowing it to continue to react at a certain rate, endowing larger incremental for the signal. The tTDN probe strategy in Fig. 5d performed better from a S/N perspective than that of triple ssDNA probes in Fig. 5c, particularly at 500 fmol, where the S/N was noticeably enhanced.

Cross-reactivity. When our requirement is the simultaneous quantitative detection of multiple components, it is a prerequisite that they will not interfere with each other's signals, and a good multi-component detection method can be used for the multiple components to be tested. The combined samples were tested and identified. We prepared a series of target gene fragments with different compositions and demonstrated its specificity by cross-reactivity experiments; the outcomes are shown in Fig. 4e. Taking the signal intensity of ^{159}Tb/^{165}Ho/^{169}Tm in the histogram as a reference, we can conclude from the results that whether it is the input of a single component RNA or the detection of any mixture of two components, or even testing the three components together, our tTDN MNAzyme nanosystem can output corresponding independent and stable results.

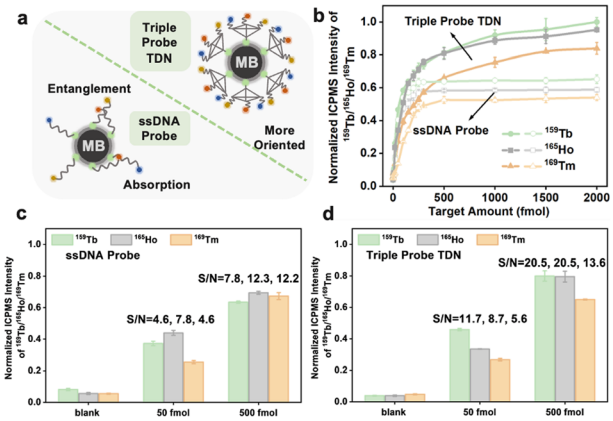

Fig. 5 (a) Schematic illustration of the sensing surface attached with ssDNA and tTDN. (b) Comparison of responses of single-probe and tTDN sensors to different concentrations of target RNA. (c) Analytical performance of the ssDNA probe and (d) triple probe and the signal-to-noise ratio at different target concentrations.

Selectivity. Variation sites often occur in a single or a few bases, resulting in a high degree of sequence homology between different RNAs, thus we conducted a series of detection of single/triple-base mismatched RNA distractions. The results are shown in Fig. 4f; it gives the corresponding mismatched RNA fragments of the three target RNA fragments HV69/70 del, K417N, and T478K. It is worth mentioning that the good single base mismatch resolution of this strategy reflects its advantages in screening variants since variants differ from the original sequence by just a few nucleotides. In addition, two common miRNAs were also determined as two cases of non-complementary fragments, which showed good selectivity for target genes due to the good recognition ability of the system.

Recoveries and determined results. In order to assess the method's applicability, healthy human throat samples were obtained by swabbing and extracted using kits; the processed samples served as substrate interference, spiked at various doses within the analytical range, and then reacted with the built method. Detailed steps are demonstrated in the ESI.†

Table 1 Analytical performance of HV69/70 del/K417N/T478K based on tTDN–MNAzyme

Target	Linear range (fmol)	Linear relationship	R^2	LOD (fmol)
HV69/70 del	5–2000	$y = 1758.1 \log(x) - 1881.6$	0.9901	1.2
K417N	5–2000	$y = 1768.2 \log(x) - 1525.5$	0.9784	1.5
T478K	5–2000	$y = 1518.1 \log(x) - 977.21$	0.9824	1.1

Table 2 Results of the standard addition recovery experiment in the virus extract

Sample	Target	Added (fmol)	Found (fmol)	Recovery (%)	RSD (%)
1#	HV69/70 del	0	Not found	—	2.9
		50	46.8	93.6	3.8
	K417N	0	Not found	—	5.6
		50	47.9	95.8	6.9
	T478K	0	Not found	—	5.6
		50	45.9	91.9	7.0
2#	HV69/70 del	0	Not found	—	3.9
		150	151.5	100.9	2.6
	K417N	0	Not found	—	1.2
		150	152.9	101.9	2.1
	T478K	0	Not found	—	2.1
		150	154.8	103.2	3.9
3#	HV69/70 del	0	Not found	—	0.7
		500	493.3	98.7	0.9
	K417N	0	Not found	—	1.7
		500	502.8	100.6	0.8
	T478K	0	Not found	—	1.4
		500	488.9	97.8	0.5

Additionally, the suggested procedure was applied to the spiked samples. The results of quantitative recovery are all given in Table 2. The matrix sample spiked recovery values ranged from 91.9 to 103.2% for varying doses. As a result, it has strengthened the case for the SARS-CoV-2 variant RNA virus extraction sample matrix's toleration and demonstrated the potential of this approach for the studies' actual use.

Conclusions

To address the general problem of the lack of multi-component ability of detection methods for SARS-CoV-2 variants, we have established an isotope encoded tTDN–MNAzyme satellite strategy. Specifically, adopting a multi-component MNAzyme reaction system operated by tTDN with rigid molecular scaffolding and multiple vertex modification properties, tTDN–MBs assembled as a satellite structure, releasing ^{159}Tb, ^{165}Ho, and ^{169}Tm lanthanide isotope tags out of orbit, corresponding to the HV69/70 del, K417N and T478K characteristic gene sites of four VOC SARS-CoV-2 variants. The established method endows a sensitivity of 1.1–1.5 fmol, and a wide quantitative range of 5–2000 fmol. We anticipate that this highly sensitive, multi-component method can be extended to more applications for high throughput detection of biological samples.

Data availability

The datasets supporting this article have been uploaded as part of the ESI.† ESI† contains detailed information of apparatus and reagents, detailed experimental protocols of AFM analysis, dynamic light scattering analysis, zeta-potential analysis, isotope labeling, PAGE, and RNA extraction. Operating parameters of ICPMS (Table S1†), nucleotide sequences (Table S2†), ESI-MS of MMA-DOTA-Ln^{3+} (Fig. S1†), MALDI-TOF-MS of DNA-MMA-DOTA-Ln^{3+} (Fig. S2†), AFM images (Fig. S3†), DLS of TDN (Fig. S4†), TEM of MBs (Fig. S5†), zeta-potential of MBs (Fig. S6†), EDS of MBs (Fig. S7†), calibration curves of isotopes in ICPMS (Fig. S8†), and optimization of experimental conditions (Fig. S9–S14†).

Author contributions

Yi Lv conceptualized the project methodology. Yi Lv and Rui Liu supervised the investigation. Ziyan Li implemented, collected and analyzed the experimental data and wrote the original manuscript. Chaoqun Wang and Jing Zhou performed the validation and sample analysis. Yi Lv, Rui Liu, and Jianyu Hu revised the manuscript.

Conflicts of interest

There are no conflicts to declare.

Acknowledgements

This work was supported by the National Natural Science Foundation of China (No. 22074098 & 22074096), the Science & Technology Department of Sichuan Province (2021ZYD0047) and the Fundamental Research Funds for the Central Universities. We thank Prof. Yunfei Tian, Dr. Xiaobo Xie and Dr. Shuguang Yan of the Analytical & Testing Center of Sichuan University for technical assistance.

References

1 W. J. Guan, Z. Y. Ni, Y. Hu, W. H. Liang, C. Q. Ou, J. X. He, L. Liu, H. Shan, C. L. Lei, D. S. C. Hui, B. Du, L. J. Li, G. Zeng, K. Y. Yuen, R. C. Chen, C. L. Tang, T. Wang, P. Y. Chen, J. Xiang, S. Y. Li, J. L. Wang, Z. J. Liang, Y. X. Peng, L. Wei, Y. Liu, Y. H. Hu, P. Peng, J. M. Wang, J. Y. Liu, Z. Chen, G. Li, Z. J. Zheng, S. Q. Qiu, J. Luo,

C. J. Ye, S. Y. Zhu and N. S. Zhong, *N. Engl. J. Med.*, 2020, **382**, 1708–1720.
2 T. P. Peacock, D. H. Goldhill, J. Zhou, L. Baillon, R. Frise, O. C. Swann, R. Kugathasan, R. Penn, J. C. Brown, R. Y. Sanchez-David, L. Braga, M. K. Williamson, J. A. Hassard, E. Staller, B. Hanley, M. Osborn, M. Giacca, A. D. Davidson, D. A. Matthews and W. S. Barclay, *Nat. Microbiol.*, 2021, **6**, 899–909.
3 S. Ramesh, M. Govindarajulu, R. S. Parise, L. Neel, T. Shankar, S. Patel, P. Lowery, F. Smith, M. Dhanasekaran and T. Moore, *Vaccines*, 2021, **9**(10), 1195.
4 J. Ou, W. Lan, X. Wu, T. Zhao, B. Duan, P. Yang, Y. Ren, L. Quan, W. Zhao, D. Seto, J. Chodosh, Z. Luo, J. Wu and Q. Zhang, *Signal Transduction Targeted Ther.*, 2022, **7**, 138.
5 M. Takeda, *Microbiol. Immunol.*, 2022, **66**, 15–23.
6 H. Yousefi, A. Mahmud, D. Chang, J. Das, S. Gomis, J. B. Chen, H. Wang, T. Been, L. Yip, E. Coomes, Z. Li, S. Mubareka, A. McGeer, N. Christie, S. Gray-Owen, A. Cochrane, J. M. Rini, E. H. Sargent and S. O. Kelley, *J. Am. Chem. Soc.*, 2021, **143**, 1722–1727.
7 C. B. Jackson, M. Farzan, B. Chen and H. Choe, *Nat. Rev. Mol. Cell Biol.*, 2022, **23**, 3–20.
8 B. Udugama, P. Kadhiresan, H. N. Kozlowski, A. Malekjahani, M. Osborne, V. Y. C. Li, H. Chen, S. Mubareka, J. B. Gubbay and W. C. W. Chan, *ACS Nano*, 2020, **14**, 3822–3835.
9 M. Gwinn, D. MacCannell and G. L. Armstrong, *J. Am. Med. Assoc.*, 2019, **321**, 893–894.
10 K. Karasawa and H. Arakawa, *Luminescence*, 2022, **37**, 822–827.
11 S. A. Byrnes, R. Gallagher, A. Steadman, C. Bennett, R. Rivera, C. Ortega, S. T. Motley, P. Jain, B. H. Weigl and J. T. Connelly, *Anal. Chem.*, 2021, **93**, 4160–4165.
12 A. Y. Trick, F. E. Chen, L. B. Chen, P. W. Lee, A. C. Hasnain, H. H. Mostafa, K. C. Carroll and T. H. Wang, *Adv. Mater. Technol.*, 2022, **7**(6), 2101013.
13 R. Liu, S. Zhang, C. Wei, Z. Xing, S. Zhang and X. Zhang, *Acc. Chem. Res.*, 2016, **49**, 775–783.
14 M. M. Aynaud, J. J. Hernandez, S. Barutcu, U. Braunschweig, K. Chan, J. D. Pearson, D. Trcka, S. L. Prosser, J. Kim, M. Barrios-Rodiles, M. Jen, S. Song, J. Shen, C. Bruce, B. Hazlett, S. Poutanen, L. Attisano, R. Bremner, B. J. Blencowe, T. Mazzulli, H. Han, L. Pelletier and J. L. Wrana, *Nat. Commun.*, 2021, **12**, 1405.
15 A. Babiker, C. W. Myers, C. E. Hill and J. Guarner, *Am. J. Clin. Pathol.*, 2020, **153**, 706–708.
16 M. M. Hernandez, R. Banu, P. Shrestha, A. S. Gonzalez-Reiche, A. van de Guchte, K. Farrugia, R. Sebra, M. R. Gitman, M. D. Nowak, C. Cordon-Cardo, V. Simon, H. van Bakel, E. M. Sordillo, N. Luna, A. Ramirez, S. A. Castaneda, L. H. Patino, N. Ballesteros, M. Munoz, J. D. Ramirez, A. E. Paniz-Mondolfi and M. S. P. S. Grp, *Microbiol. Spectrum*, 2022, **10**(5), e01736–22.
17 R. J. Dikdan, S. A. E. Marras, A. P. Field, A. Brownlee, A. Cironi, D. A. Hill and S. Tyagi, *J. Mol. Diagn.*, 2022, **24**, 309–319.
18 G. Han, S. Zhang, Z. Xing and X. Zhang, *Angew. Chem., Int. Ed. Engl.*, 2013, **52**, 1466–1471.
19 J. Hu, R. Liu, J. Zhou and Y. Lv, *Chem. Sci.*, 2021, **12**, 13404–13412.
20 X. W. Zhang, M. X. Liu, M. Q. He, S. Chen, Y. L. Yu and J. H. Wang, *Anal. Chem.*, 2021, **93**, 6437–6445.
21 Z. Li, X. Chen, Z. Huang, J. Zhou, R. Liu and Y. Lv, *Anal. Chem.*, 2021, **93**, 12714–12722.
22 Z. Q. Deng, J. Y. Hu, R. Liu and Y. Lv, *At. Spectrosc.*, 2022, **43**, 201–206.
23 Y. Zhou, S. Yuan, K. K. To, X. Xu, H. Li, J. P. Cai, C. Luo, I. F. Hung, K. H. Chan, K. Y. Yuen, Y. F. Li, J. F. Chan and H. Sun, *Chem. Sci.*, 2022, **13**, 3216–3226.
24 C. Q. Wang, Z. Q. Deng, H. Zhang, R. Liu and Y. Lv, *Chin. Chem. Lett.*, 2022, **33**, 1267–1270.
25 G. Han, M. H. Spitzer, S. C. Bendall, W. J. Fantl and G. P. Nolan, *Nat. Protoc.*, 2018, **13**, 2121–2148.
26 Z. Y. Yuan, Q. M. Zhou, L. S. Cai, L. Pan, W. L. Sun, S. W. Qumu, S. Yu, J. X. Feng, H. S. Zhao, Y. C. Zheng, M. L. Shi, S. Li, Y. Chen, X. R. Zhang and M. Q. Zhang, *Nat. Methods*, 2021, **18**, 1223.
27 M. Lin, J. Wang, G. Zhou, J. Wang, N. Wu, J. Lu, J. Gao, X. Chen, J. Shi, X. Zuo and C. Fan, *Angew. Chem.*, 2015, **127**, 2179–2183.
28 J. Wang, D. X. Wang, J. Y. Ma, Y. X. Wang and D. M. Kong, *Chem. Sci.*, 2019, **10**, 9758–9767.
29 R. P. Goodman, I. A. Schaap, C. F. Tardin, C. M. Erben, R. M. Berry, C. F. Schmidt and A. J. Turberfield, *Science*, 2005, **310**, 1661–1665.
30 J. Yan, Z. Zhang, X. Zhan, K. Chen, Y. Pu, Y. Liang and B. He, *Nanoscale*, 2021, **13**, 9577–9589.
31 J. Li, K. Xun, L. Zheng, X. Peng, L. Qiu and W. Tan, *J. Am. Chem. Soc.*, 2021, **143**, 4585–4592.
32 D. Wang, S. Li, Z. Zhao, X. Zhang and W. Tan, *Angew. Chem., Int. Ed. Engl.*, 2021, **60**, 15816–15820.
33 X. Chen, J. Huang, S. Zhang, F. Mo, S. Su, Y. Li, L. Fang, J. Deng, H. Huang, Z. Luo and J. Zheng, *ACS Appl. Mater. Interfaces*, 2019, **11**, 3745–3752.
34 H. Pei, X. Zuo, D. Zhu, Q. Huang and C. Fan, *Acc. Chem. Res.*, 2014, **47**, 550–559.
35 P. He, W. Han, C. Bi, W. Song, S. Niu, H. Zhou and X. Zhang, *ACS Nano*, 2021, **15**, 6961–6976.
36 F. Li, Y. Liu, Y. Dong, Y. Chu, N. Song and D. Yang, *J. Am. Chem. Soc.*, 2022, **144**, 4667–4677.
37 Y. Yang, C. Song, J. Zhang, J. Chao, H. M. Luong, Y. Zhao and L. Wang, *Nanoscale*, 2022, **14**, 4538–4547.
38 Q. Wang, Z. He, H. Zhu, W. Gao, N. Zhang, J. Li, J. Yan, B. He and X. Ye, *J. Mater. Chem. B*, 2022, **10**, 438–449.
39 L. Chen, S. Luo, Z. Ge, C. Fan, Y. Yang, Q. Li and Y. Zhang, *Nano Lett.*, 2022, **22**, 1618–1625.
40 R. Peng, X. Zheng, Y. Lyu, L. Xu, X. Zhang, G. Ke, Q. Liu, C. You, S. Huan and W. Tan, *J. Am. Chem. Soc.*, 2018, **140**, 9793–9796.
41 M. Lin, P. Song, G. Zhou, X. Zuo, A. Aldalbahi, X. Lou, J. Shi and C. Fan, *Nat. Protoc.*, 2016, **11**, 1244–1263.
42 P. Peng, Y. Du, J. Zheng, H. Wang and T. Li, *Angew. Chem., Int. Ed. Engl.*, 2019, **58**, 1648–1653.

43 T. Zhang, T. Tian and Y. Lin, *Adv. Mater.*, 2021, e2107820, DOI: **10.1002/adma.202107820**.
44 Q. Kang, M. He, B. Chen, G. Xiao and B. Hu, *Anal. Chem.*, 2021, **93**, 737–744.
45 J. Zhuang, J. Tan, C. Wu, J. Zhang, T. Liu, C. Fan, J. Li and Y. Zhang, *Nucleic Acids Res.*, 2020, **48**, 8870–8882.
46 X. Yan, L. Yang and Q. Wang, *Angew. Chem., Int. Ed. Engl.*, 2011, **50**, 5130–5133.
47 S. Wang, M. Xia, J. Liu, S. Zhang and X. Zhang, *ACS Sens.*, 2017, **2**, 735–739.
48 P. Miao, B. Wang, X. Chen, X. Li and Y. Tang, *ACS Appl. Mater. Interfaces*, 2015, **7**, 6238–6243.